

Abstract

[Predicting the spatiotemporal distribution of rainfall remains a key challenge in Tropical Meteorology, partly due to an incomplete understanding of the effects of different environmental factors on atmospheric convection. In this work, we use numerical simulations of tropical ocean domains to study how rainfall responds to imposed localized thermal and mechanical forcings to the atmosphere. We use the Normalized Gross Moist Stability—NGMS—to quantify the net precipitation response associated with a given net atmospheric heating. We find that NGMS values differ considerably for different forcings, but show that the relationship between precipitation and column relative humidity collapses along a universal curve across all of them. We also show that the contributions from mean vertical advection of moist and dry static energy only approximate the NGMS well at scales larger than a couple hundred kilometers, indicating that general horizontal mixing processes are not negligible at smaller scales.

]

Plain Language Summary

[Predicting where rain tends to occur in tropical areas is challenging. In this work, we simulate a small area of atmosphere over a tropical ocean to study how rainfall changes when we alter the surface temperature, the atmospheric heating rate at different heights, and the pressure gradients that drive the winds near the surface. We find that such alterations lead to self-consistent but different relationships between the amount of rainfall produced and the net heating of the atmosphere. We show that the spatial extent of the alteration affects how well this relationship can be inferred from horizontally-averaged atmospheric properties. In contrast, we find that the relationship between rainfall and the average relative humidity in the atmosphere remains the same across all types of environmental alterations.]

1 Introduction

What makes it rain where it does in the tropics? Two distinct, influential paradigms often invoked to answer this question are those proposed by Lindzen and Nigam (1987), and by Neelin and Held (1987). Lindzen and Nigam argued that maxima in precipitation are controlled by low-level wind convergence that is mechanically forced by boundary-layer pressure gradients associated with sea-surface temperature—SST—patterns. On the other hand, Neelin and Held posited that maxima of deep convection and rainfall are regulated by a combination of the net column energy input, and the “Gross Moist Stability” (GMS) – a metric of how efficiently ascending circulations export this energy surplus. These are representative of what we refer to subsequently as “mechanical” and “column-energetic” schools of thought. These schools are united in the importance they assign to determining patterns of vertical motion, which regulate atmospheric moisture import and thus the amount by which local precipitation exceeds local evaporation. In this work, we use idealized simulations to examine the impacts of both mechanical and column-energetic (or thermodynamic) forcings on precipitation. We focus on scales ranging from tens to a few hundred kilometers, given their significant relevance for human communities and ecosystems, and the size constraints of simulations at cloud- and cloud-system-resolving scales.

The success of column-energetic arguments in accounting for large-scale precipitation patterns and zonal-mean shifts is well-documented (Donohoe et al., 2013; Marshall et al., 2014; Bischoff & Schneider, 2014; Schneider et al., 2014; Boos & Korty, 2016). However, establishing the value of the GMS in advance poses a singular challenge for predictive uses of the column-energetic approach. Additionally, its explanatory power fails for phenomena at finer scales, for instance the behavior of the narrow East-Pacific In-

62 terropical Convergence Zone (ITCZ) (Sobel & Neelin, 2006; Back & Bretherton, 2006),
 63 or precipitation over small islands in idealized models (Cronin et al., 2015). Furthermore,
 64 the column-energetic view does little to explain rainfall maxima over orography, which
 65 provide critical water supplies for billions of people. In these contexts, the contribution
 66 of mechanically induced convergence, ignored by column energetics, seems to play a piv-
 67 otal role.

68 Several modeling studies have explored the sensitivity of deep convection and rain-
 69 fall to forcings of different kinds. Derbyshire et al. (2004) used a CRM with adjusted dry-
 70 ing at different heights, allowing the model to relax to a prescribed profile of relative hu-
 71 midity, and found that a strong drying in the mid-troposphere suppressed deep convec-
 72 tion and led to shallow convection. Using a CRM under the Weak Temperature Gradi-
 73 ent approximation (WTG), Wang and Sobel (2012) found that mid- and lower-tropospheric
 74 drying led to lower precipitation than upper-tropospheric drying. In turn, Anber et al.
 75 (2015) separately prescribed heating throughout the depth of the atmospheric column,
 76 and surface enthalpy flux anomalies, and showed that, while the former led to more pre-
 77 cipitation for forcings close to the RCE reference, total precipitation responded more sen-
 78 sitivity to changes in surface enthalpy fluxes than to atmospheric heating, per change
 79 in W/m^2 of forcing.

80 In this letter, we study how different thermodynamic and mechanical mechanisms
 81 affect time-mean rainfall at scales of tens to a few hundred kilometers. We run numer-
 82 ical simulations of convection over idealized ocean domains in a CRM, where we intro-
 83 duce three types of forcings, illustrated in Figure 1:

- 84 • Localized SST anomalies,
- 85 • vertically and horizontally localized heating at different heights,
- 86 • mechanical forcing of the horizontal winds consistent with localized convergence.

87 We use these forcings as an idealized way of separately probing how phenomena such as
 88 aerosol-induced warming at different levels, narrow regions of high SST, or wind conver-
 89 gence induced by orography or large-scale circulations, affect tropical rainfall patterns.
 90 We characterize the effects of the forcings, and discuss the implications of analyzing their
 91 behavior in terms of two metrics of the Gross Moist Stability, and the relationship be-
 92 tween precipitation and column moisture. We also assess how the spatial scale of the forc-
 93 ings affects both rainfall and the properties of the ascending circulations over the forced
 94 patch.

95 2 Methods

96 We perform numerical simulations in radiative-convective equilibrium using the Sys-
 97 tem for Atmospheric Modeling, SAM (Khairoutdinov & Randall, 2003), version 6.10.6.
 98 The basic setup consists of a domain over an ocean surface that is doubly-periodic in the
 99 horizontal, with 1024 by 32 grids in the horizontal at 3 km spacing, and a stretched grid
 100 with 64 vertical levels. We use the same parameterization schemes as Cronin et al. (2015),
 101 and initialize our runs from profiles of temperature and humidity in radiative-convective
 102 equilibrium (RCE) with an all-ocean surface.

103 For all simulations performed, perturbations are prescribed over or along the edges
 104 of a reference patch region that spans the whole short dimension of the channel, and has
 105 half-width of 24 km in the long dimension (unless indicated otherwise). The surface is
 106 allowed to evaporate freely, and its temperature is fixed at 300.2 K, except for the SSTA
 107 simulations described below. We follow Cronin (2014) in prescribing a solar latitude of
 108 45° and a solar constant of 560 Wm^{-2} and a zenith angle of 56.26° , which yield an in-
 109 solation of 311 Wm^{-2} . To prevent convective aggregation, all of our runs homogenize
 110 radiation across the domain. We perform three main groups of forced simulations (Fig-

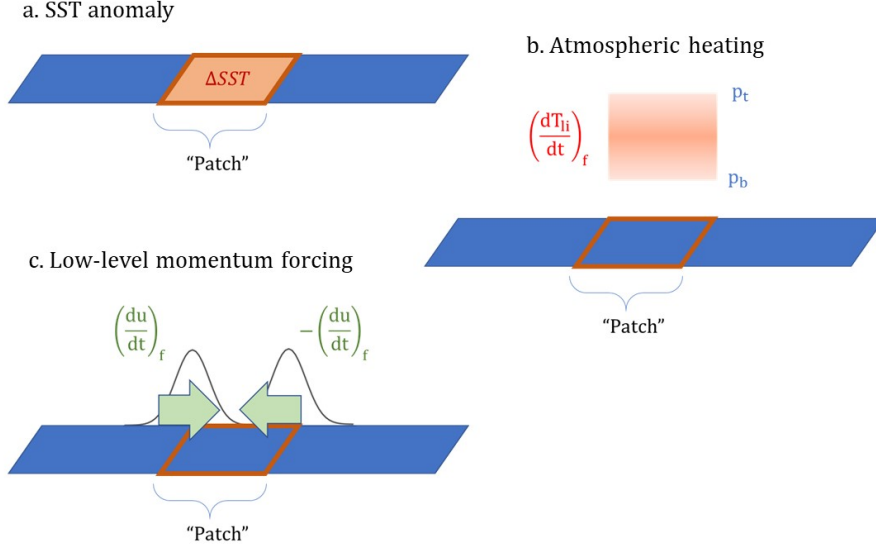


Figure 1. Sketches of the setups representing the three different forcings: a. Sea-surface temperature anomaly, b. Atmospheric heating between levels p_b and p_t , c. Low-level momentum forcing. The reference patch for which averages are calculated is indicated in red; geometry is not to scale.

111 ure 1). All of our simulations are run for 75 days, with the last 50 days used for the anal-
 112 ysis.

113 **2.1 Numerical Experiment 1: SST anomalies**

114 For the first set of simulations, denoted by SSTA, we prescribe a constant surface
 115 temperature anomaly for the area of the patch given by $SST(x, y) = T_0 + \Delta T$ if (x, y)
 116 are contained within the patch, and T_0 otherwise, where $T_0 = 300.2$ K is the reference
 117 surface temperature. We run simulations with ΔT taking values of $-0.4, -0.1, 0.1, 0.4, 0.7, 1.0, 1.5$
 118 and 2.0 K. We note that the temperature anomaly as prescribed here is discontinuous
 119 at the edge of the reference patch—as is the heating forcing discussed in the next sec-
 120 tion. However, tests run with other profiles did not produce dramatically different re-
 121 sults. No pathological behavior was observed from the sharp discontinuities.

122 **2.2 Numerical Experiment 2: Localized atmospheric heating at differ-
 123 ent levels**

124 To assess the convective response to heating at different levels, we add a forcing
 125 term Q to the equation for the liquid water/ice static energy h_{li} :

$$\frac{dh_{li}}{dt}(p, t) = (\dots) + Q \quad (1)$$

126 For the forcing, we choose a half-sinusoidal shape in the vertical, constrained between
 127 two pressure levels, uniform values in the horizontal within the patch region, and zero
 128 outside.

$$Q = M \sin\left(\pi \frac{p - p_t}{p_b - p_t}\right) \quad (2)$$

129 where M is the maximum amplitude of the forcing, p is the pressure, and p_t and p_b are
 130 the pressure levels at the top and at the bottom of the heated layer, respectively. This

131 yields an expression for M in terms of the integrated column forcing, Q_f , namely

$$M = \frac{g\pi Q_f}{2c_p(p_b - p_t)}, \quad (3)$$

132 obtained from the mass-weighted integral of $c_p Q$ in the vertical. For instance, $Q_f = 1 \text{ W/m}^2$
 133 corresponds to $M = 2.05 \cdot 10^{-7} \text{ K/s}$. We perform simulations with values of Q_f of $-10, -5, 5, 10, 20, 40$
 134 and 50 W/m^2 , and apply the thermal forcings at four different levels:

- 135 • Qlb: $p_b = 1000 \text{ hPa}, p_t = 900 \text{ hPa}$,
- 136 • Qlt: $p_b = 900 \text{ hPa}, p_t = 800 \text{ hPa}$,
- 137 • Qm: $p_b = 700 \text{ hPa}, p_t = 400 \text{ hPa}$,
- 138 • Qu: $p_b = 500 \text{ hPa}, p_t = 200 \text{ hPa}$,

139 which represent the boundary layer, the lower free troposphere, and mid- and upper-tropospheric
 140 layers, respectively.

141 2.3 Numerical Experiment 3: Low-level wind forcing

142 The last set of numerical simulations examines the effects of purely mechanical low-
 143 level convergence on rainfall over the patch region without forced thermal gradients in
 144 the boundary layer. To do this, we introduce a forcing F_m in the along-channel compo-
 145 nent (x) of the momentum equation, namely

$$\frac{du}{dt} = (\dots) + F_m \quad (4)$$

146 For simplicity, we assume a Gaussian-shaped distribution for the forcing, centered at each
 147 border of the strip (x_0), with standard deviation σ_m of 12 km, and a vertical decay scale
 148 h_l of 500 m. That is,

$$F_m(x, z) = \beta \exp\left(-\frac{(x - x_0)^2}{2\sigma_m^2}\right) \exp\left(\frac{-z}{h_l}\right) \quad (5)$$

149 Where β is the maximum imposed acceleration. F_m can be interpreted as an additional
 150 pressure gradient force, and its integral, through Bernoulli's principle, can be interpreted
 151 as a maximum consequent inflow speed in the absence of friction.

$$\int_{-\infty}^{\infty} F_m dx = -\frac{\Delta P}{\rho} = \frac{u_{max}^2}{2} \quad (6)$$

152 Here, ΔP represents the equivalent pressure drop that the forcing would produce. ρ is
 153 the air density. This relationship allows us to relate the forcing strength β to a maxi-
 154 mal convergent wind speed u_{max} :

$$\beta = \frac{u_{max}^2}{2\sigma_m \sqrt{2\pi}} \quad (7)$$

155 We perform momentum forcing simulations, denoted by MF, using values of u_{max} set
 156 at $-2, -1, 1, 2, 3, 5, 7$ and 10 m/s , where the negative values signify an imposed tendency
 157 for winds to blow out of the patch. We note that, while β and u_{max} do not depend on
 158 h_l , h_l is expected to affect the strength of rainfall by modulating the depth of the con-
 159 vergent flow.

160 Our approach in the MF simulations provides a convenient way to induce conver-
 161 gence mechanically without prescribing a mean background wind or fixing the low-level
 162 convergence. The simple geometry of our simulations does not intend to capture the full
 163 complexity of particular scenarios of mechanically driven convergence, such as those of
 164 flow over orography. However, previous work on simulations of idealized tropical islands
 165 with simple orography and a mean background wind has shown substantial precipita-
 166 tion enhancement for a wide range of imposed background wind speeds (Wang & Sobel,
 167 2017).

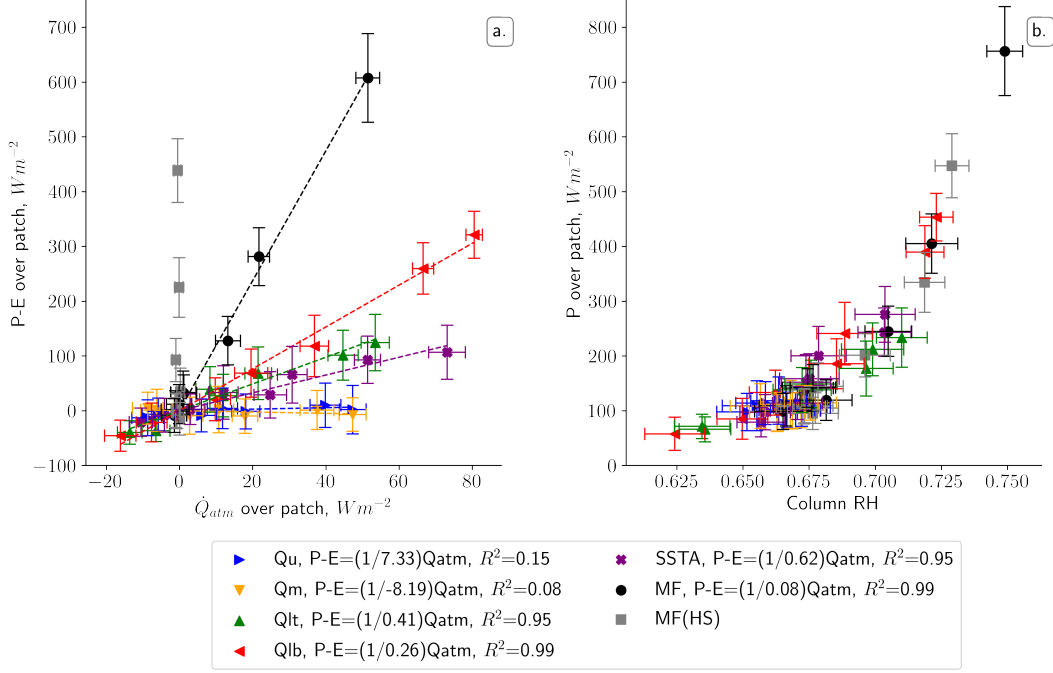


Figure 2. (a) $P - E$ vs. \dot{Q}_{atm} over reference patch for simulations forced with atmospheric heating (triangles), SST anomaly (purple exes), low-level momentum (black circles), and low-level momentum with homogenized surface fluxes (gray squares; MF(HS)). For Qlb, Qlt, SSTA and MF, a linear fit is shown whose slope corresponds to the NGMS. Error bars indicate ± 2 standard errors of the mean of daily values. (b) Precipitation vs. mean atmospheric column relative humidity—CRH—over reference patch.

3 Results

3.1 Different convective responses to different forcings

All surface and low-level forcings, namely SSTA, Qlb, Qlt and MF, result in a significant response in $P-E$, the precipitation minus evaporation or “net precipitation”, over the reference patch, as shown in Figure 2. In contrast, imposed mid- and upper-level heating produces negligible changes in $P-E$. This finding agrees with Wang and Sobel (2012), who showed a weaker sensitivity of precipitation responses to drying anomalies in the upper troposphere in WTG simulations over oceans.

Our simulations also show that low-level forcings produce different responses in $P-E$ over the patch, as indicated by the slopes of the lines in figure 2a. Following Raymond et al. (2009), we define the Normalized Gross Moist Stability—NGMS henceforth—as the quantity mediating the relationship between the column-integrated atmospheric heating rate or entropy forcing, \dot{Q}_{atm} , and net precipitation $P-E$. The entropy forcing is calculated as $\dot{Q}_{atm} = LHF + SHF + \dot{Q}_{rad} + Q_f$, where LHF and SHF are the surface latent and sensible heat fluxes, respectively, \dot{Q}_{rad} is the radiative heating rate, and Q_f is the imposed heating. Denoting the NGMS by Γ_R , we write

$$P - E = \frac{1}{\Gamma_R} \dot{Q}_{atm}. \quad (8)$$

A higher value of NGMS indicates thus a less efficient conversion of the net column-integrated heating into net precipitation.

186 A central result of this work is that the net precipitation response to distinct types
 187 of low-level forcings results in distinct values of NGMS. A forcing-dependent NGMS is
 188 reasonably well-defined for each type of low-level forcing because $P-E$ varies linearly
 189 with \dot{Q}_{atm} . The linearity of convective responses to transient as well as steady pertur-
 190 bations to the SST and the atmospheric water vapor has been shown in previous simu-
 191 lation based on the Weak Temperature Gradient approximation (Kuang, 2012; Wang
 192 & Sobel, 2012; Anber et al., 2015; Kuang, 2018; Beucler et al., 2018), but, to the best
 193 of our knowledge, not for RCE with localized forcings.

194 For simulations with added column heating, the prescribed forcing, Q_f , must be
 195 distinguished from the total entropy forcing or atmospheric heating rate \dot{Q}_{atm} , which
 196 includes the atmospheric feedback on the imposed heating. This feedback is composed
 197 of changes in the latent, sensible and radiative heat fluxes from the RCE state. Although
 198 Q_f represents the main contribution to \dot{Q}_{atm} for simulations with atmospheric heating,
 199 surface flux feedbacks contribute up to 40 percent of the entropy forcing in the simula-
 200 tions with heating at the lowest levels (Qlb). For both SSTA and MF, \dot{Q}_{atm} is dominated
 201 by changes in the latent heat flux, with sensible heat fluxes accounting for 20 to 30 per-
 202 cent of the total.

203 The change in precipitation induced by low-level forcings is strongly associated with
 204 changes in the column relative humidity (CRH), as indicated in Figure 2b. Previous ob-
 205 servational studies of tropical rainfall have documented an approximately exponential
 206 relation between precipitation and CRH (Bretherton et al., 2004; Peters & Neelin, 2006;
 207 Rushley et al., 2018; Martinez-Villalobos & Neelin, 2019), namely $P = P_0 \exp(A \cdot \text{CRH})$,
 208 where A corresponds to the e-folding growth rate, and P_0 is a constant. We note that
 209 an exponential fit to our simulations (not shown) yields an e-folding growth rate of \sim
 210 21, higher than the value of ~ 15 documented by observational studies (Bretherton et
 211 al., 2004; Rushley et al., 2018). A mechanistic explanation of this well-documented re-
 212 lationship between P and CRH is currently lacking, although our findings suggest that
 213 it holds for mechanical as well as thermodynamic forcings.

214 3.2 Vertical profiles and Gross Moist Stability

215 The magnitude and structure of the mean vertical velocity profile over the patch,
 216 \bar{w} , is key to understanding the contrast in precipitation response across different simu-
 217 lations. Low-level forcings, namely SSTA, MF, Qlb and Qlt, show \bar{w} profiles with two
 218 peaks: one at lower levels, localized at or close to the location of the forcing, and one
 219 in the free troposphere indicating a deep convective response (Figure 3, a. through c.).
 220 In contrast, forcings in the mid- and upper troposphere, Qm and Qu, only produce lo-
 221 cal responses in \bar{w} .

222 The interaction between the profiles of \bar{w} and moist static energy (MSE) offers a
 223 key to understand the precipitation responses in our simulations. The MSE is given by
 224 $h = c_p T + gz + L_v q$, where c_p is the specific heat capacity of air at constant pressure,
 225 T is the temperature, g is the gravitational acceleration, z is the height, L_v is the latent
 226 heat of vaporization of water, and q is the specific humidity. In particular, the vertical
 227 gradient of MSE over the domain, $\partial \bar{h} / \partial z$, indicates the locations where energy is imported
 228 into or exported out of the atmospheric column. For all low-level forcings, the low-level
 229 circulations include ascent at heights where $\frac{\partial \bar{h}}{\partial z} < 0$, which implies a net low-level MSE
 230 import and its associated instability. This net import requires in turn an energy export
 231 mechanism: this occurs both through the development of the deep circulation, which has
 232 a positive GMS and thus helps export energy to the rest of the domain, and through lat-
 233 eral mixing (not quantified).

234 Are the vertical velocity profiles consistent with our expectations based on required
 235 thermodynamic and momentum balances for each forcing? For simulations with local-
 236 ized atmospheric column heating, if the convective heating were unchanged by the ad-

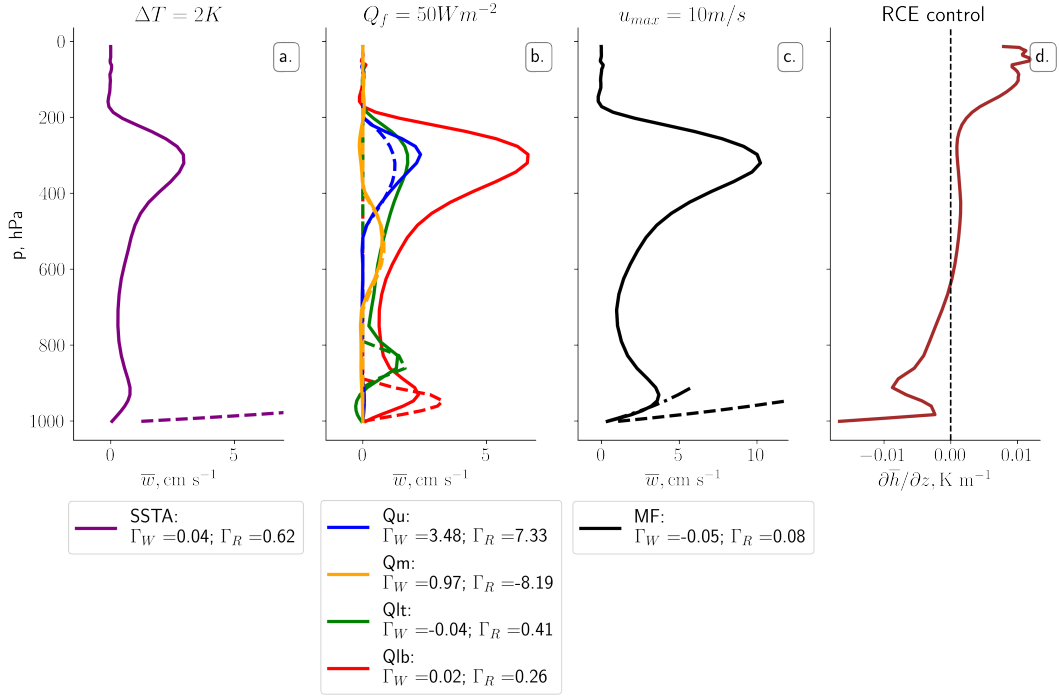


Figure 3. (a-c) Profiles of mean vertical velocity over the reference patch for sea-surface temperature, atmospheric heating, and momentum forcings with the highest magnitudes simulated. Dashed lines represent hypothesized profiles of w based on Bernoulli’s principle and mass continuity (for SSTA and MF), and on WTG for atmospheric heating simulations (see text). Dashed-dotted line for MF shows the estimate based on the vertical profile of the forcing and the actual velocity at the patch border. (d) Vertical profile of vertical MSE gradient for the control simulation in RCE. Legend indicates the vertical GMS, Γ_V , and the NGMS, Γ_R (see text).

237 dition of the forcing, then the WTG vertical velocity:

$$w_{WTG} = \frac{\dot{Q}_f}{ds/dz}, \quad (9)$$

238 would be a good model for how w responds to forcing. In the equation, \dot{Q}_f is the forc-
 239 ing between the pressure levels specified for each simulation, and ds/dz is the vertical
 240 gradient of dry static energy—given by $s = c_p T + gz$ —averaged over the depth between
 241 such pressure levels, and over the extent of the patch. Figure 3b offers a contrast between
 242 the mean vertical velocity profile over the patch, and the equivalent w_{WTG} velocities calcu-
 243 lated according to equation 9, for simulations with atmospheric column heating at dif-
 244 ferent levels with magnitude of 50Wm^{-2} . The WTG-inferred vertical velocities capture
 245 well the local vertical velocities at the levels where the forcings are prescribed. It is sur-
 246 prising that w_{WTG} works so well in cases that couple strongly to deep convection, like
 247 Qlb and Qlt, because there the total convective heating is clearly altered, yet the local
 248 (in height) convective heating is not greatly modified. The deep convective responses to
 249 the low-level forcings are not captured by w_{WTG} , as expected.

250 Previous work has found that forcings with steady temperature tendencies (Kuang,
 251 2010) as well as with transient temperature anomalies (Tulich & Mapes, 2010; Tian &
 252 Kuang, 2019) produce locally confined responses when applied to the upper troposphere,
 253 and deep convective responses when applied to the lower troposphere. Using a linear re-

254 sponse framework and Lagrangian tracking, Tian and Kuang (2019) linked these differ-
 255 ing responses primarily to the effects of the anomalies on the vertical velocity of updrafts
 256 and on their buoyancy, with only a secondary contribution from the changes in liquid
 257 water content of the air parcels. Despite some qualitative similarity, we note that our
 258 simulations prescribe heating tendencies, and not transient temperature anomalies, and
 259 that they are constrained horizontally as well as vertically. Further study is thus needed
 260 to assess if the mechanisms are similar.

261 For the momentum forcing simulation with $u_{max} = 10\text{m/s}$, we obtain a physically-
 262 based null model of the \bar{w} profile for the lowermost 100 hPa by equating the pressure gra-
 263 dient forcing to an equivalent wind convergence through Bernoulli's principle, and in-
 264 tegrating the mass continuity equation (see derivation in the Supplement). The null model
 265 is at best an upper bound to the horizontal winds, as it neglects friction, as well as feed-
 266 backs from cold pools over the reference patch, resulting in a large overestimation of the
 267 time-mean ascent through the depth of the mixed layer (Figure 3c). We note that there
 268 is high temporal variability in the ascent over the patch, and the null model does pro-
 269 vide a good upper bound for the strongest circulations at low levels (not shown).

270 To obtain an analogous null-model for vertical velocity at low levels for SSTA with
 271 $\Delta T = 2\text{K}$, we proceed similarly to MF, with the added assumption that the air tem-
 272 perature difference between the patch and the surroundings is constant and equal to ΔT
 273 through the depth of the mixed layer (see Supplement). This gives a corresponding pres-
 274 sure difference profile, which, similarly as for MF, yields an expected \bar{w} of approximately
 275 11 cm s^{-1} at 950 hPa, much higher than the simulated mean. This discrepancy is largely
 276 due to the boundary-layer temperature anomalies varying between -0.1K and 0.15K in
 277 the lowest kilometer of the atmosphere, a much smaller contrast than the imposed SST
 278 anomaly. This is crucial, as gradients in boundary layer temperatures, and particularly
 279 their Laplacian, have been shown to play a central role in the patterns of surface con-
 280 vergence in the tropics (Duffy et al., 2020). For both SSTA and MF simulations, our re-
 281 sults indicate that stabilizing feedbacks on the near-surface pressure gradients tend to
 282 weaken the ascent profile considerably.

283 From the budgets of moist static energy and latent energy, it can be shown that
 284 $\Gamma_R = \frac{\nabla \cdot \langle \bar{v}h \rangle}{\nabla \cdot \langle \bar{v}(s-h) \rangle}$ (see the Supplement for a derivation). However, it is common—and
 285 often convenient—to approximate Γ_R by the contribution from the vertical transport of
 286 MSE and dry static energy by the mean vertical circulations only (Sobel, 2007; Wang
 287 & Sobel, 2012; Anber et al., 2015). This approximate NGMS, denoted here by Γ_W and
 288 given by $\Gamma_W = \frac{\langle \bar{w} \partial h / \partial z \rangle}{\langle \bar{w} \partial (s-h) / \partial z \rangle}$, neglects the contributions from both vertical transients
 289 and horizontal transport terms. Horizontal transport could be neglected on the grounds
 290 that horizontal gradients in both h and s are normally weak, but this need not always
 291 be the case. In fact, this is likely not justified for our patches of 24 km half-widths: as
 292 indicated in the legend to Figure 3, Γ_W shows poor correspondence with the values of
 293 Γ_R . The strength and structure of low-level ascent relative to upper-tropospheric ascent
 294 modulates Γ_W , but Γ_W does not correlate strongly with Γ_R for these patch sizes (Fig-
 295 ure 3), indicating that the effects of transients or horizontal transport—or both—are key
 296 in determining the exact value of Γ_R for each forcing.

297 3.3 Patch size effects

298 We also test the effects of varying the spatial scales on net precipitation by run-
 299 ning additional simulations with patches of half-widths 48, 96 and 192 km, for the SSTA
 300 and MF forcings, shown in Figure 4. We note that atmospheric heating simulations tended
 301 to aggregate convection for larger patch sizes and strong forcings, and were thus not in-
 302 cluded.

303 The behavior of $P - E$ with SST anomaly does not change substantially for dif-
 304 ferent sizes for the range of anomalies considered, although the spread reaches up to 70 Wm^{-2}
 305 for the strongest forcing. For the momentum forcing it does exhibit wider spread, since
 306 the forcing is applied over the same area while the patch is made larger, leading to a de-
 307 crease in low-level convergence. The patch size increases cause the theoretical low-level
 308 convergence to scale by a factor of $1/L$, with L denoting the half-width. However, the
 309 curves do not collapse when $P - E$ is plotted against u_{max}/L , indicating other effects
 310 are at play.

311 We have established that Γ_W is not a good approximation to the NGMS for a scale
 312 of 24 km. However, as the patch is made wider, this discrepancy decreases: for SSTA,
 313 the relative error between them drops from close to 100 percent at 24 km, to under 5 per-
 314 cent at 192 km. For MF, it drops from 200 percent at 24 km, to about 6 percent at 192
 315 km. This indicates that the net contribution from transients and horizontal transport
 316 of moist and dry static energy becomes negligible at a few hundred kilometers, but plays
 317 a major role at small scales.

318 The values of the NGMS for SSTA do not show a clear trend as the patch is made
 319 wider, suggesting that net precipitation does not depend monotonically on the size of
 320 the region with anomalous SST. In contrast, a slight but monotonic increase is observed
 321 for MF simulations, with the lowest NGMS at the smallest scales. This is consistent with
 322 low-level wind convergence driving enhanced rainfall and weakening with increased patch
 323 area for fixed u_{max} .

324 4 Discussion

325 We have found well-defined values of NGMS for different types of low-level forc-
 326 ing imposed. This suggests that we could in principle provide reasonable estimates for
 327 $P - E$ for a given forcing magnitude by interpolating from others. However, the neces-
 328 sity of knowing the NGMS a priori, as well as the substantial variations in NGMS be-
 329 tween different types of forcings, severely limit the applicability of the column energetic
 330 perspective of Neelin and Held (1987) in predicting precipitation on the basis of envi-
 331 ronmental forcings. For instance, simulations with mechanically-induced convergence and
 332 homogenized surface fluxes show greatly enhanced rainfall over patches with near-zero
 333 net atmospheric heating rates.

334 Our results also show that a prescribed heating in the middle and upper troposphere
 335 (above about 700 hPa) does not lead to significant net precipitation enhancement. This
 336 is a reminder that knowledge of the total atmospheric column heating rate does not nec-
 337 essarily provide useful information about $P - E$, unless we know how that energy in-
 338 put is distributed in the vertical. The use of a vertically integrated column-energetic bud-
 339 get might overestimate the effectiveness of upper-level heating in driving deep convec-
 340 tion, and underestimate the capacity of low-level wind convergence to do the same.

341 Our simulations provide evidence that Γ_W , which only takes into account the ef-
 342 fects of vertical transport of moist and dry static energy by the mean vertical circula-
 343 tions, is a poor approximation to the NGMS in most of our forcings at scales of 24 km,
 344 but improves substantially at scales of a few hundred kilometers. However, the scale at
 345 which Γ_W becomes a reasonable approximation of Γ_R is likely to vary depending on the
 346 characteristics of low-level convergence. Horizontal MSE transport in particular has been
 347 shown to contribute significantly to the full NGMS in relatively narrow areas such as the
 348 East Pacific ITCZ (Back & Bretherton, 2006, 2009).

349 Although studying convective enhancement at large scales without homogenizing
 350 radiation would be desirable, it poses the challenge that large domains in RCE produce
 351 convective self-aggregation if radiation is made interactive (Muller & Bony, 2015; Wing
 352 et al., 2018).

353 Previous studies have hypothesized that precipitation rates over tropical oceans are
 354 governed by the mean moisture saturation deficit of the troposphere, and hence by the
 355 CRH (Raymond, 2000; Raymond et al., 2009). Satellite-based observations have since
 356 confirmed a close relationship between precipitation and CRH (Bretherton et al., 2004;
 357 Peters & Neelin, 2006; Rushley et al., 2018). However, recent theoretical frameworks for
 358 tropical moist convection have argued that such relationship can be explained as a con-
 359 sequence of the effect of rainfall on environmental humidity via convective moisture de-
 360 trainment, or that both precipitation and CRH are affected simultaneously by other causes,
 361 such as large-scale ascent and column energetics (Emanuel, 2019; Singh et al., 2019).

362 Our simulations show that large-scale ascent associated with column energy export,
 363 as well as ascent associated with mechanically-induced convergence, can both increase
 364 CRH. Hence, the dependence of precipitation on CRH is agnostic to the distinction be-
 365 tween mechanical and thermodynamic forcings in our simulations, and is likely not merely
 366 due to both variables co-varying with column energetics. This hints at a plausible causal
 367 link between them, although more evidence and a mechanistic explanation would be needed
 368 to settle the matter.

369 5 Conclusion

370 Motivated by the goal of understanding the mechanisms that govern rainfall in the
 371 tropics at human-relevant spatial scales, we have explored how different kinds of ther-
 372 modynamic and mechanical forcings affect precipitation rates in idealized cloud-resolving
 373 simulations of a tropical atmospheric domain. Our results indicate that the Normalized
 374 Gross Moist Stability, which mediates the relationship between atmospheric heating and
 375 net rainfall, is well defined within simulations with low-level forcings, such as localized
 376 sea-surface temperature anomalies, low-level atmospheric heating, and mechanically-induced
 377 horizontal winds that converge onto a reference area, but varies substantially from one
 378 type of forcing to another. Despite their differences in NGMS, our simulations collapse
 379 onto the same curve of precipitation versus column relative humidity. This suggests that
 380 the mechanisms that maintain this relationship deserve more attention.

381 6 Open Research

382 Processed simulation data and scripts are available in the Zenodo repository with
 383 DOI:10.5281/zenodo.10086216 (Velez-Pardo, 2023).

384 References

- 385 Anber, U., Wang, S., & Sobel, A. (2015). Effect of surface fluxes versus radiative
 386 heating on tropical deep convection. *Journal of the Atmospheric Sciences*,
 387 *72*(9), 3378–3388.
- 388 Back, L. E., & Bretherton, C. (2006). Geographic variability in the export of moist
 389 static energy and vertical motion profiles in the tropical pacific. *Geophysical*
 390 *research letters*, *33*(17).
- 391 Back, L. E., & Bretherton, C. S. (2009). On the relationship between sst gradi-
 392 ents, boundary layer winds, and convergence over the tropical oceans. *Journal*
 393 *of Climate*, *22*(15), 4182–4196.
- 394 Beucler, T., Cronin, T., & Emanuel, K. (2018). A linear response framework for
 395 radiative-convective instability. *Journal of Advances in Modeling Earth Sys-*
 396 *tems*, *10*(8), 1924–1951.
- 397 Bischoff, T., & Schneider, T. (2014). Energetic constraints on the position of the in-
 398 tertropical convergence zone. *Journal of Climate*, *27*(13), 4937–4951.
- 399 Boos, W. R., & Korty, R. L. (2016). Regional energy budget control of the in-
 400 tertropical convergence zone and application to mid-holocene rainfall. *Nature*

- 401 *Geoscience*, 9(12), 892–897.
- 402 Bretherton, C. S., Peters, M. E., & Back, L. E. (2004). Relationships between wa-
 403 ter vapor path and precipitation over the tropical oceans. *Journal of climate*,
 404 17(7), 1517–1528.
- 405 Cronin, T. W. (2014). On the choice of average solar zenith angle. *Journal of the*
 406 *Atmospheric Sciences*, 71(8), 2994–3003.
- 407 Cronin, T. W., Emanuel, K. A., & Molnar, P. (2015). Island precipitation enhance-
 408 ment and the diurnal cycle in radiative-convective equilibrium. *Quarterly Jour-*
 409 *nal of the Royal Meteorological Society*, 141(689), 1017–1034.
- 410 Derbyshire, S., Beau, I., Bechtold, P., Grandpeix, J.-Y., Piriou, J.-M., Redelsperger,
 411 J.-L., & Soares, P. (2004). Sensitivity of moist convection to environmental
 412 humidity. *Quarterly Journal of the Royal Meteorological Society: A journal*
 413 *of the atmospheric sciences, applied meteorology and physical oceanography*,
 414 130(604), 3055–3079.
- 415 Donohoe, A., Marshall, J., Ferreira, D., & Mcgee, D. (2013). The relationship
 416 between itcz location and cross-equatorial atmospheric heat transport: From
 417 the seasonal cycle to the last glacial maximum. *Journal of Climate*, 26(11),
 418 3597–3618.
- 419 Duffy, M. L., O’Gorman, P. A., & Back, L. E. (2020). Importance of laplacian
 420 of low-level warming for the response of precipitation to climate change over
 421 tropical oceans. *Journal of Climate*, 33(10), 4403–4417.
- 422 Emanuel, K. (2019). Inferences from simple models of slow, convectively coupled
 423 processes. *Journal of the Atmospheric Sciences*, 76(1), 195–208.
- 424 Khairoutdinov, M. F., & Randall, D. A. (2003). Cloud resolving modeling of the
 425 arm summer 1997 iop: Model formulation, results, uncertainties, and sensitivi-
 426 ties. *Journal of the Atmospheric Sciences*, 60(4), 607–625.
- 427 Kuang, Z. (2010). Linear response functions of a cumulus ensemble to temperature
 428 and moisture perturbations and implications for the dynamics of convectively
 429 coupled waves. *Journal of the atmospheric sciences*, 67(4), 941–962.
- 430 Kuang, Z. (2012). Weakly forced mock walker cells. *Journal of the Atmospheric Sci-*
 431 *ences*, 69(9), 2759–2786.
- 432 Kuang, Z. (2018). Linear stability of moist convecting atmospheres. part i: From
 433 linear response functions to a simple model and applications to convectively
 434 coupled waves. *Journal of the Atmospheric Sciences*, 75(9), 2889–2907.
- 435 Lindzen, R. S., & Nigam, S. (1987). On the role of sea surface temperature gradi-
 436 ents in forcing low-level winds and convergence in the tropics. *Journal of At-*
 437 *mospheric Sciences*, 44(17), 2418–2436.
- 438 Marshall, J., Donohoe, A., Ferreira, D., & McGee, D. (2014). The ocean’s role in
 439 setting the mean position of the inter-tropical convergence zone. *Climate Dy-*
 440 *namics*, 42, 1967–1979.
- 441 Martinez-Villalobos, C., & Neelin, J. D. (2019). Why do precipitation intensities
 442 tend to follow gamma distributions? *Journal of the Atmospheric Sciences*,
 443 76(11), 3611–3631.
- 444 Muller, C., & Bony, S. (2015). What favors convective aggregation and why? *Geo-*
 445 *physical Research Letters*, 42(13), 5626–5634.
- 446 Neelin, J. D., & Held, I. M. (1987). Modeling tropical convergence based on the
 447 moist static energy budget. *Monthly Weather Review*, 115(1), 3–12.
- 448 Peters, O., & Neelin, J. D. (2006). Critical phenomena in atmospheric precipitation.
 449 *Nature physics*, 2(6), 393–396.
- 450 Raymond, D. J. (2000). Thermodynamic control of tropical rainfall. *Quarterly Jour-*
 451 *nal of the Royal Meteorological Society*, 126(564), 889–898.
- 452 Raymond, D. J., Sessions, S. L., Sobel, A. H., & Fuchs, Z. (2009). The mechanics of
 453 gross moist stability. *Journal of Advances in Modeling Earth Systems*, 1(3).
- 454 Rushley, S. S., Kim, D., Bretherton, C., & Ahn, M.-S. (2018). Reexamining the non-
 455 linear moisture-precipitation relationship over the tropical oceans. *Geophysical*

- 456 *research letters*, 45(2), 1133–1140.
- 457 Schneider, T., Bischoff, T., & Haug, G. H. (2014). Migrations and dynamics of the
458 intertropical convergence zone. *Nature*, 513(7516), 45–53.
- 459 Singh, M. S., Warren, R. A., & Jakob, C. (2019). A steady-state model for the rela-
460 tionship between humidity, instability, and precipitation in the tropics. *Journal*
461 *of Advances in Modeling Earth Systems*, 11(12), 3973–3994.
- 462 Sobel, A. H. (2007). Simple models of ensemble-averaged tropical precipitation and
463 surface wind, given the sea surface temperature. *The global circulation of the*
464 *atmosphere*, 219, 251.
- 465 Sobel, A. H., & Neelin, J. D. (2006). The boundary layer contribution to intertrop-
466 ical convergence zones in the quasi-equilibrium tropical circulation model
467 framework. *Theoretical and Computational Fluid Dynamics*, 20, 323–350.
- 468 Tian, Y., & Kuang, Z. (2019). Why does deep convection have different sensitivities
469 to temperature perturbations in the lower versus upper troposphere? *Journal*
470 *of the Atmospheric Sciences*, 76(1), 27–41.
- 471 Tulich, S. N., & Mapes, B. E. (2010). Transient environmental sensitivities of explic-
472 itly simulated tropical convection. *Journal of the atmospheric sciences*, 67(4),
473 923–940.
- 474 Velez-Pardo, M. (2023). *Accompanying data for "the response of tropical rainfall to*
475 *idealized small-scale thermal and mechanical forcing", by martin velez-pardo*
476 *and timothy w. cronin* [dataset]. Zenodo. Retrieved from [https://doi.org/](https://doi.org/10.5281/zenodo.10086216)
477 [10.5281/zenodo.10086216](https://doi.org/10.5281/zenodo.10086216) doi: 10.5281/zenodo.10086216
- 478 Wang, S., & Sobel, A. (2012). Impact of imposed drying on deep convection in
479 a cloud-resolving model. *Journal of Geophysical Research: Atmospheres*,
480 117(D2).
- 481 Wang, S., & Sobel, A. H. (2017). Factors controlling rain on small tropical islands:
482 Diurnal cycle, large-scale wind speed, and topography. *Journal of the Atmo-*
483 *spheric Sciences*, 74(11), 3515–3532.
- 484 Wing, A. A., Emanuel, K., Holloway, C. E., & Muller, C. (2018). Convective self-
485 aggregation in numerical simulations: A review. *Shallow clouds, water vapor,*
486 *circulation, and climate sensitivity*, 1–25.

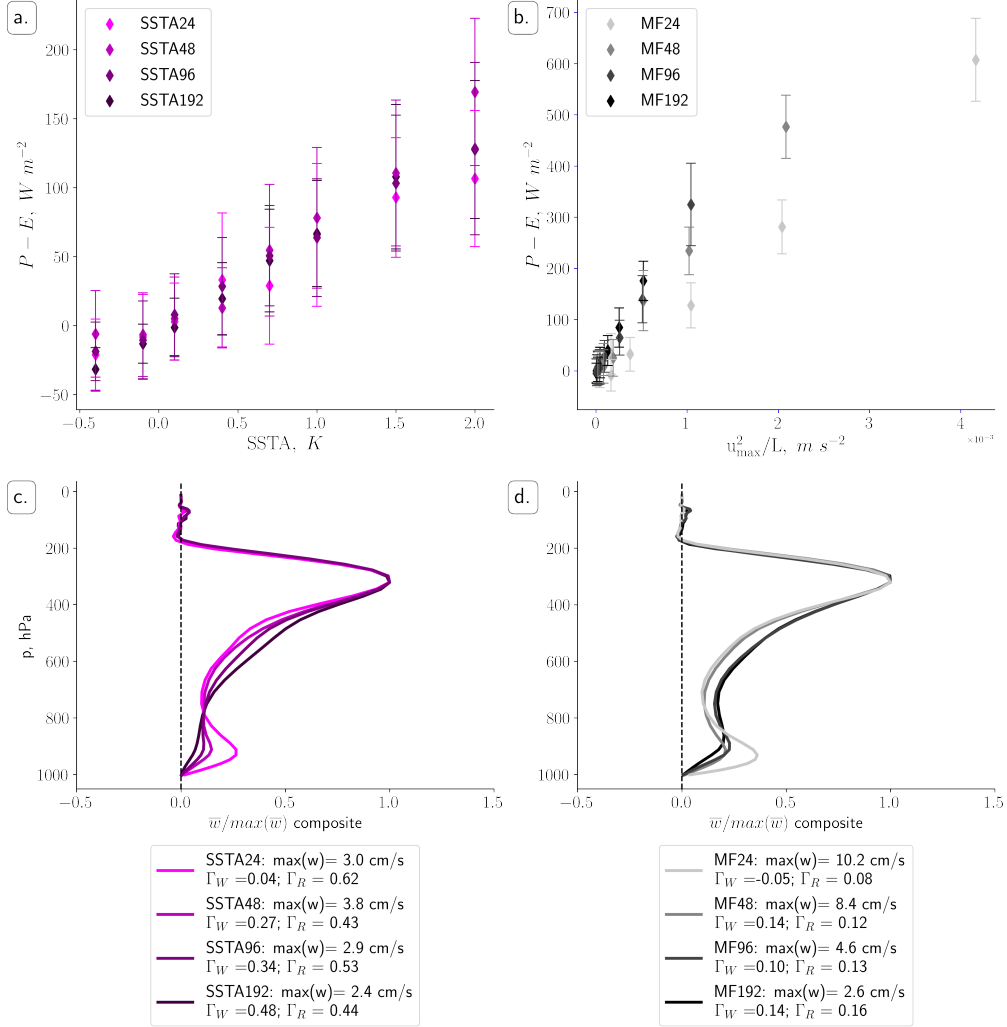


Figure 4. (Top row) Scatter plots of $P - E$ vs. sea-surface temperature anomaly (a.) and the square of the momentum forcing parameter u_{max} divided by patch half-width (b.) for patches of half-widths 24, 48, 96 and 192 km. (Bottom row) Vertical profiles of normalized mean vertical velocities for patches of half-widths of 24, 48, 96 and 192 km for SST anomaly of 2K (c.) and momentum forcing with $u_{max} = 10m/s$ (d.). The legend indicates the maximum value of vertical velocity used for normalization, as well as the NGMS (Γ_R) and its approximated form (Γ_W ; see text).